Engineering Research Express

PAPER

Damage recovery for SRF photoinjector cavities

Yegor Tamashevich[1], **Axel Neumann**[1], **Andre Frahm**[1], **Frank Göbel**[1], **Sascha Klauke**[1], **Alexander Matveenko**[1], **Henry Plötz**[1], **Alena Prudnikava**[1], **Ivo Rudolph**[1], **Michael Schuster**[1], **Jan Ullrich**[1] **and Jens Knobloch**[1,2]

[1] Helmholtz Centre for Materials and Energy, D-12489 Berlin, Germany
[2] Department of Physics, Universität Siegen, Walter-Flex-Str. 3, 57068 Siegen, Germany

E-mail: yegor.tamashevich@helmholtz-berlin.de

Keywords: niobium, superconducting cavity, niobium oxide, mechanical polishing, x-ray photoelectron spectroscopy, high-pressure water rinsing, hydrofluoric acid rinsing

OPEN ACCESS

RECEIVED
21 August 2023

REVISED
23 October 2023

ACCEPTED FOR PUBLICATION
18 April 2024

PUBLISHED
7 May 2024

Abstract

Two niobium elliptical 1.3 GHz superconducting radio frequency (SRF) electron photoinjector cavities were successfully recovered after mechanical inner surface damage. Both cavities had deep imprints in the critical high surface electric field area around the photoelectric cathode position. The lengthy repair procedure, which consists of surface inspection and defect characterization, mechanical polishing and light chemical etching is described in detail. In the process, a new high pressure rinsing (HPR) nozzle system optimized for the special photoinjector geometry was also developed. Subsequent cold RF tests demonstrate complete performance recovery. This is the first time that photoinjector cavities damaged in the high electric-field region could be recovered.

1. Introduction

Helmholtz-Zentrum Berlin (HZB) is currently designing and building a high-average current all superconducting continuous wave (CW) driven energy recovery linear accelerator (ERL) as a prototype to demonstrate low normalized beam emittance of better than 1 mm × mrad at up to 100 mA and short pulses of about 2 ps. In order to achieve these demanding goals HZB started a staged program for developing high current, high brightness SRF electron sources [1].

1.1. Photoinjector cavity design

The SRF photoinjector cavity is the most critical component of the electron injector. In order to mitigate risk of a failed design, it is being developed in several stages. The cavity design described here is the first stage towards the final high power version. The 1.4-cell design features a short half-cell optimized for low emittance beam dynamics and dark current mitigation and a rather narrow cathode channel. It is equipped with an insert of a high quantum efficiency (QE) normal-conducting multi-alkali cathode [2].

An overview of the cavity is given in figure 1. The 1.4-cell cavity includes a choke cell (2) and an enlarged beam tube (6) to allow higher order modes (HOM) above the fundamental TM_{010} monopole mode to propagate to the absorber following the downstream coupler port (5) and superconducting solenoid. The cavity is equipped with a blade tuner [3], featuring a stepper motor for coarse tuning and piezo stacks for fine tuning. For operation up to 4 mA beam current, the cavity is equipped with two modified EU XFEL power couplers optimized for CW operation [4] capable of 10 kW CW RF power each. The field distribution of the fundamental mode of the Gun RF cavity was chosen to optimise for a low beam emittance and at the same time allow for a high average current acceleration of 10 mA.

Whereas the emittance requires a high electric field for immediate acceleration at the cathode to prevent emittance growth by space charge effects within the electron bunch, the high current limits the field by the RF power requirements. The design is a compromise of fairly high field during emission to prevent space charge driven emittance growth, while the limit by total beam power transferred through the power couplers results in a beam energy between 2.0 and 2.6 MeV.

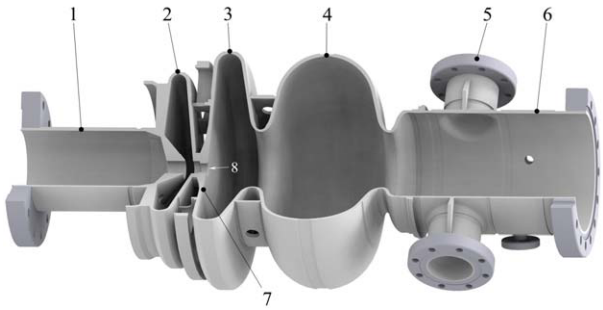

Figure 1. SRF photoinjector cavity. 1—cathode tube, 2—choke cell, 3—half-cell, 4—main cell, 5—two input coupler ports, 6—beam tube, 7—back wall, 8—opening for cathode.

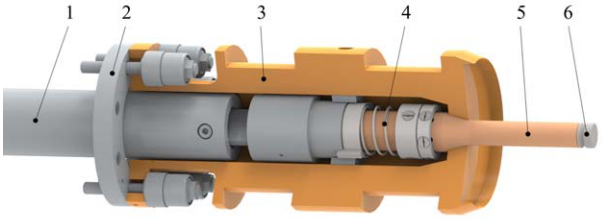

Figure 2. Cathode insert design: 1—transfer rod (is out of the cavity, when cathode is at target position and locked), 2—thermal and electrical insulating ceramics, 3—Petrov filter, 4—bayonet spring, 5—cathode insert, 6—cathode plug.

The field distribution was optimized such that the on-axis field has its maximum as close as possible to the cathode, but not on the cathode itself. This helps to minimize the danger of field emission (FE) and results in radial field components for initial focussing [5].

1.2. Cathode-insert design

The cathode insert and exchange mechanism (see figure 2) is a variant of the Helmholtz-Zentrum Dresden-Rossendorf (HZDR) design [6] with the main difference, that the cathode plug is kept in place by a mechanism exerting force by a special copper-beryllium spring (not shown) fixing the molybdenum plug (6) on the copper insert (5). The cathode is cooled via helium gas to 80 K with thermal transfer between the cooling jacket (not shown), the copper-made Petrov filter (3) and the insert itself to the plug. The Petrov filter acts as an additional RF filter to the choke cell to suppress any fundamental mode propagation downstream the cathode transfer mechanism and match the impedances. The transfer rod (1) is removed after cathode transfer, when the bayonet mechanism locks the insert into the inner Petrov filter channel.

2. Cavities description

There were two photoinjector cavities built at this stage: Gun 1.0 and Gun 1.1. The present work describes treatment of both cavities.

2.1. Gun 1.0

The Gun 1.0 prototype cavity was built by Jefferson Laboratory. The as-produced half-cell was 5 mm shorter than the design which results in heavy multipacting when the maximum on-axis (E_0) field exceeds 17 MV m^{-1}. For the same reason the cavity's fundamental frequency was lowered by about 1.5 MHz. Gun 1.0 was retreated (buffered chemical polishing and high-pressure rinsing) many times but always had strong field emission. This cavity was used for the first cold cathode experiment at HZB. Gun 1.0 was assembled into a cold string and installed in the Gun Lab - a test cryomodule equipped with a diagnostic beam line to characterise the electron beam [7].

In figure 3 an intrinsic quality factor Q_0 [8], a measure proportional to the inverse of the resonator's surface resistance, is plotted versus maximum on-axis field E_0. The plot shows evolution of the cavity performance starting from initial fabrication acceptance test (final vertical test) to a test of the complete beam vacuum system

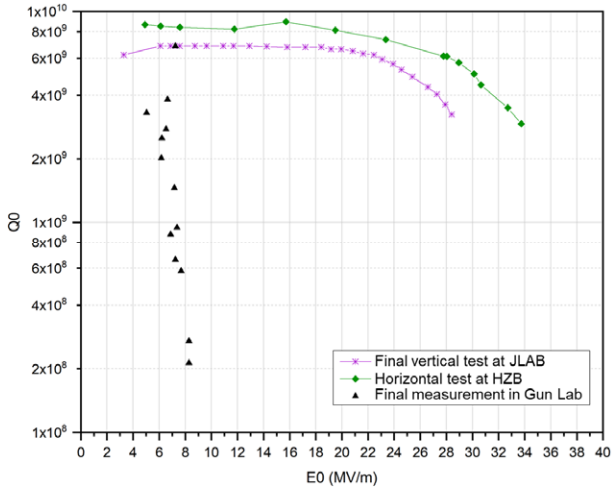

Figure 3. Gun 1.0 performance in intrinsic quality factor Q_0 versus on-axis peak electric field of the TM010-π mode at different stages of operation.

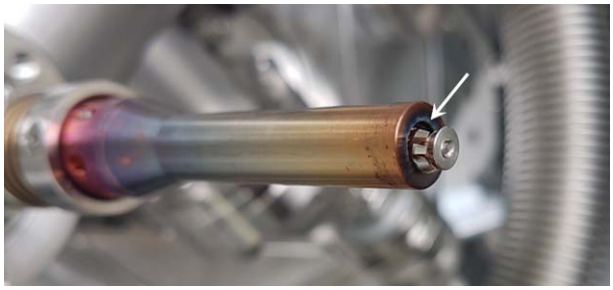

Figure 4. Copper cathode insert covered with a sputtered material (pointed with an arrow). The missing lip of the holding mechanism can be noted close to the arrow.

assembled in the cleanroom with the cavity, the so-called cold-string horisontal test, until the last run in the Gun Lab with photo-cathode transferred towards the half-cell's back wall opening.

The cryomodule operation has demonstrated a large dark current even without a cathode installed [9]. RF operation was also performed with a copper cathode and demonstrated a significant cavity quality factor degradation (black triangles in figure 3). Furthermore, multipacting and field emission occurred at very low field levels of 8 MV m^{-1} E_0, which could even not be suppressed by a DC bias voltage up to 9 kV. Later the cathode insert was found to be covered with cathode sputtered material (see figure 4) caused presumably by discharges in the gap between the cathode plug and the insert. This material deposited on the niobium surface of the cavity is the main candidate to explain the quality factor degradation. Also, during one of the cathode exchanges, the cathode insert was damaged. One lip of the holding spring was broken (missing lip can be noted in figure 4). During release of the transfer rod from the insert, the molybdenum cathode plug fell into the half cell. Subsequently, the cavity had to be disassembled from the module for cathode removal and cavity repair.

2.1.1. Removing the cathode

The cavity was dismounted from the Gun Lab and transported to the clean room keeping the horizontal orientation to avoid cathode movement. The inner surface of the cavity was inspected with a camera. The cathode plug resting in the half-cell is shown in figure 5(a). It was considered too risky for the cavity surface to try to grab the cathode with any clamping device. The cathode was extracted from the cavity by means of a solidifying resin used for the cavity surface replicas (described in section 3). A flexible polyvinyl chloride (PVC) tube was positioned above the cathode plug and premixed replica material was supplied to fill the volume on the backside of the plug. The tube position was kept constant until the resin solidified and bound the tube to the cathode plug. The cathode after extraction with attached solid resin and a transparent PVC tube are shown in figure 5(b).

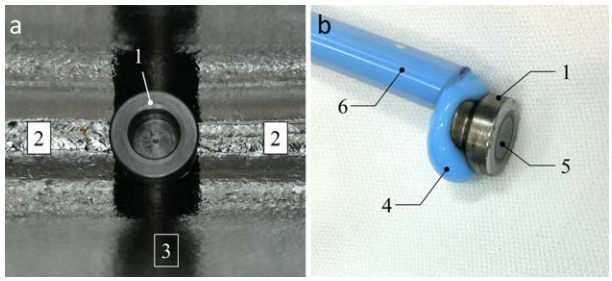

Figure 5. (a) Molybdenum cathode plug (1) resting on the equator welding seam (2) of the half-cell (running left to right). The dark vertical line (3) is a reflection artefact. (b) The extracted cathode (1) with PVC tube (6) and solid resin (4) attached. The deposited high quantum-efficiency cathode is visible on the plug face(5).

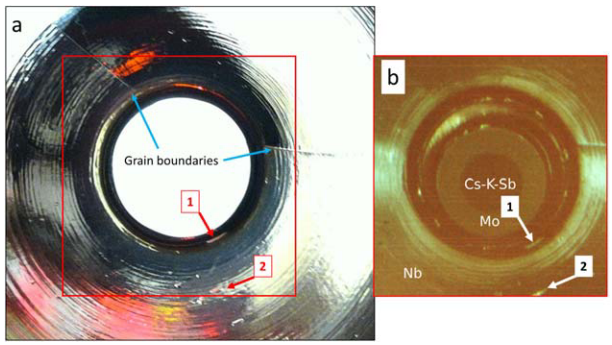

Figure 6. The optical image of the back-wall during cavity inspection (a) and the optical image of the cathode inside the cavity after the cathode transfer (b) [10]. Defects are pointed with arrows and numbers. Grain boundaries are also indicated. The dark circle in the middle is due to the cathode material coating.

After the cathode was removed, the surface optical inspection by means of a high resolution camera did not reveal any visible scratches or indents at the cathode resting position. On the other hand, high reflective spots were observed around the cathode opening. In figure 6(a) two of these spots are pointed at by the arrows and will be referred later as Defect #1 and Defect #2. The image of the same area of the cavity and the cathode shown in figure 6(b) was taken during the Gun Lab operation after the cathode transfer but before it was detached [10].

Clearly, both defects were present before the cavity test in Gun Lab. Defects were not recognised among other reflections due to poor image quality provided by a long-focus camera used to control the cathode position during the cold test.

To provide more information about the defects a replica of the surface in this region was taken as described in section 3.

2.2. Gun 1.1

Gun 1.1 is a second photoinjector cavity for the bERLinPro injector built by Research Instruments, taking into account the lessons learned from Gun 1.0 production and operation. Gun 1.1 was vertically tested before helium vessel integration as a reference for the later tests and reached $E_0 = 28.5$ MV m^{-1} without field emission (initial cavity performance is shown in figure 26, grey circles in the lower plot). The titanium tank was then successfully welded. However during final high pressure water rinsing (HPR, [11, 12]) the cavity back plate near the cathode opening collided with the HPR nozzle head. Subsequently the gun was transported to HZB for the surface inspection to gauge the extent of the damage and to evaluate repair options.

An optical image of the defects is shown in figure 7. The same replica procedure as for Gun 1.0 (see section 3) was applied to study the defect in details.

3. Cathode-area replica

A well-known [13–15] replica technique was used to acquire a detailed imprint of the cavity surface. As was demonstrated in [16] performing a replica does not influence the cavity performance provided it is completely

Figure 7. Optical image of Gun 1.1 back plate after collision with HPR nozzle. The dark area around the defect is a reflection of a camera.

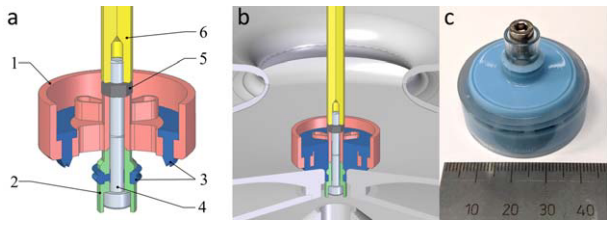

Figure 8. (a) Gun replica tool: 1 - main body, 2- pin, 3 - sealing lines, 4 - M4 screw, 5 - nut, 6—rod; (b) filled replica inside the cavity; (c) replica removed from the cavity. The screw extends beyond the tube only because it is pushed up as the assembly is resting on a table.

removed from the surface. A standard high pressure rinsing (HPR) (6 passes with 10 mm min^{-1} axial velocity and two revolutions per minute) of the surface is enough after the replica procedure.

Since HPR cannot clean the choke cell efficiently, it was essential that no replica leaks into this through the cathode opening. Hence a tool shown in figure 8(a) was developed to produce the imprint. It consists of two 3D-printed plastic parts: a main body (1) and a pin (2). Both parts are attached with a stainless steel M4 screw (4) to a plastic rod (6) which is used to position the tool and extract it from the cavity. Before the assembly, both parts were installed in the casting moulds to form sealing lines (3) with replica material.

To produce a replica the cavity was positioned vertically inside the cleanroom and the bottom of the replica tool was inserted into the cathode opening and lightly pressed against the surface. Pre-shaped double sealing lines ensure that no replica fluid leaks into the choke cell and outward the tool area on the back-plate. Mixed replica fluid (Technosil NT® duplicating silicone) was supplied from the top via hose to fill the inner volume of the tool (see figure 8(b)). After the mixture solidifies, the tool was extracted from the cavity by pulling the rod. As a result, the exact cast of the cathode opening and the area around was acquired (figure 8(c)).

4. Surface analysis

The replicas subsequently were studied in detail with a confocal laser scanning microscope (Keyence VK200) to acquire the profile of the negative. As a result, high resolution images and a 3D profile of the surface were acquired. Defects down to 0.3 μm can be resolved.

4.1. Surface defect in Gun 1.0

In figure 9 surface profiles (solid lines) of one of the replicas from Gun 1.0 are shown. Three profiles passing through the cavity axis were taken at different azimuthal angles for data redundancy (note the break in X axis). The dashed circles represent the fitted curvature of a bevel of the cathode opening. By design, the bevel radius is 2.0 mm before the chemical etching. A measured radius of 1.7 mm means that about 300 μm of material was removed in this region by etching, which was double of the average material removed based on vendor reports (about 150 μm). This effect is anticipated as during the etching all the acid is pumped through the cathode opening and thus has a much higher velocity comparing to other cavity regions. As a result, more material is

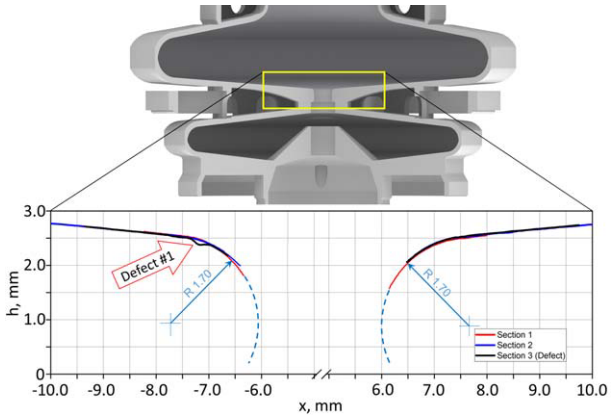

Figure 9. Surface profiles of a replica. Three sections of the same replica at different azimuthal angles are shown. Dashed circles represent fitted curvature of a bevel. Position of Defect #1 is indicated.

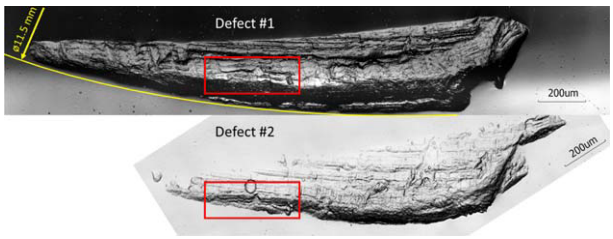

Figure 10. High resolution laser image of Defect #1 (top) and Defect #2 (bottom). The red rectangles show areas with common shape. The yellow arc marker in the top image has a diameter of 11.5 mm.

removed and the cathode opening diameter is about 0.5 mm larger than designed. Section 3 (black line) passes Defect #1 (see figure 6), so one can see the location and dimensions of the defect. Unfortunately, it is located in the region of the highest surface electric field.

High resolution images of Defect #1 and Defect #2 are shown in figure 10. One observed a similar size and shape for both defects. Furthermore, the red rectangles indicate areas with almost identical pattern, and it is probable that both defects were made by the same 'tool'. The outer edges of the defects are almost circular. The yellow arc in top image fits the outer edge of the defect and has the diameter of 11.5 mm. Defect#1 has the maximum depth of 80 μm and Defect#2 has the depth of 20 μm.

The sharp edges of the defects indicate that the damage was done after the final chemical treatment. However, the cavity producer was unable to identify the tool and the procedure which could lead to such defects.

4.2. Surface defect in gun 1.1

The defect caused by colliding with an HPR nozzle is shown in figure 11. The defect (1) has the diameter of 20 mm, maximum depth of 30 μm and maximum width of 0.8 mm. One can also see several point-like defects (2) which are not related to HPR nozzle collision, and typical etching pits (3) inherent in BCP process of single-crystal niobium.

5. Cavity retreatment

To restore the performance of cavities it was decided to remove the defects. Several options were considered. If the standard chemical treatment was chosen at least 80 μm on average must be removed by electropolishing to sufficiently smooth the defect. It would result in an unacceptable lowering of frequency (shift of about 800 kHz), which would have removed Gun 1.0 even further off target resonance frequency. In case of buffered chemical polishing (BCP) average removal and the frequency shift would be even higher [17]. However, as both cavities were integrated with helium vessels there was no possibility to tune the cavity frequency enough after surface etching. In addition, the amount of etching required would introduce a lot of hydrogen into the niobium resulting in a possible Q-disease effect [8] and quality factor degradation.

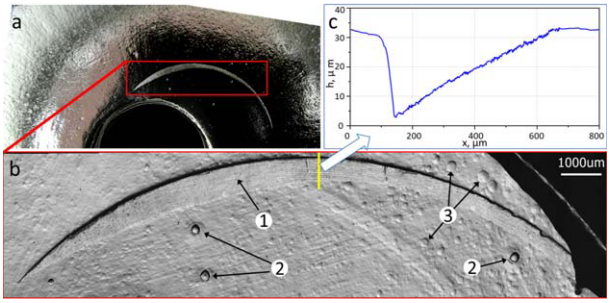

Figure 11. Optical image of the surface defect in Gun 1.1 (a), high resolution laser image of the defect (2) and its profile (c).

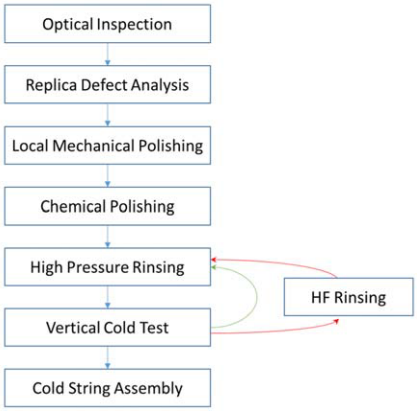

Figure 12. Retreatment workflow chart. Eventually, HF Rinsing was added as an intermediate step after vertical testing to remove oxides introduced by the high pressure rinsing.

Therefore, we decided to perform local mechanical polishing of defects followed by very light BCP (max. 10 μm) of a whole cavity and high pressure rinsing (HPR) afterwards. A workflow chart of the full retreatment procedure is shown in figure 12. Hydrofluoric acid (HF) rinsing was added afterwards to remove oxidization caused by HPR (see section 10).

Before retreatment, Gun 1.0 was rinsed with a standard HPR and tested vertically (see figure 16) to have a base-line performance.

6. Mechanical polishing procedure

The polishing procedure was developed for Gun 1.0 to prove the reliability and later was also implemented with Gun 1.1. The gun cavity was positioned vertically with a beam-tube pointing up (see figure 13) in the local clean-room to avoid contamination by foreign particles beyond the polishing media. To prevent polishing media leakage into the choke cell a plug (5) made of the same replica material was installed from the back side into the cathode opening. The plug was retracted ca 5 mm from the back-plane to provide space for the polishing tool. In addition, a protective sleeve (1) was developed to prevent any damage of the cavity inner surface by the tooling. It houses LED lights and lips for a centring ring (3). The insert is fixed to the cavity flange and gives a solid support for the polishing tool. The polishing tool consists of a plastic rod (2) and a clamp for the standard polishing heads (4). It is also equipped with the centering ring (3) to keep its position close to the cavity axis and is set in motion with a battery driven drill.

Shank-mounted felt polishing bobs of different sizes and shapes were used with ready-to-use water-solvable diamond polishing slurry Hyprez® (manufactured by Engis Corporation). The polishing was performed in three stages, each subsequent step with reduced grain size of the polishing media: 14 μm, 8 μm and 3 μm. The grain size was selected according to [18] and adjusted based on the defect size and our experience of Nb metallographic sample preparation. The view of the polishing bob above the back wall is shown in figure 14. After each step, the cavity back-plate was sprayed with deionised water to dilute the slurry. The slurry with water was removed by means of a PVC hose connected to a vacuum cleaner. The cleaning procedure was repeated several times before

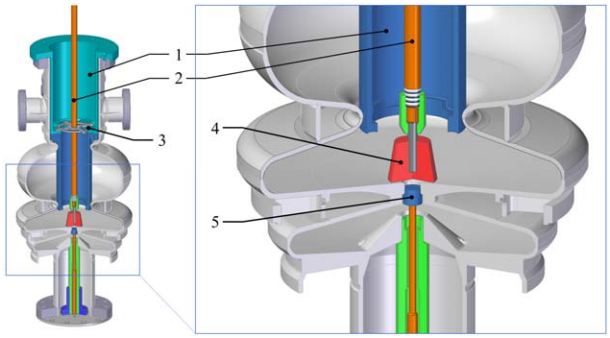

Figure 13. Gun polishing setup: 1—protective insert, 2—rotating shaft, 3—centering ring, 4—polishing bob, 5—plug.

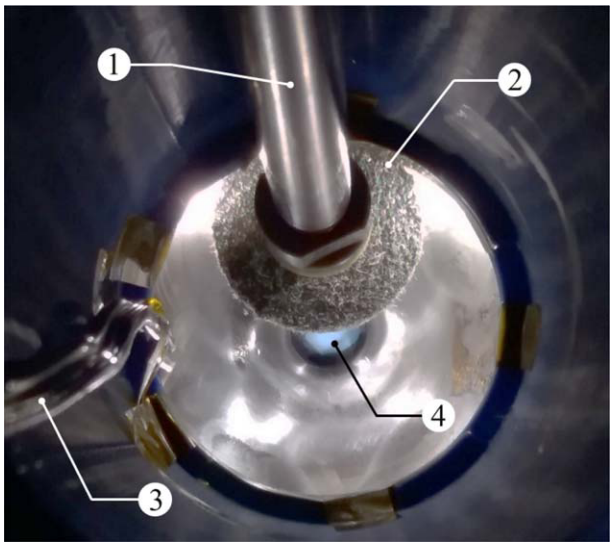

Figure 14. The view from the top beam tube opening down towards the end plate of the half cell: 1—shaft, 2—polishing bob, 3—plastic hose for draining and spraying. The plug (4) is installed in the cathode opening.

switching to smaller grain size polishing. Individual polishing heads were used for every grain size to avoid scratches at a finer polishing step.

The evolution of the surface is shown in figure 15.

7. Chemical etching

After the mechanical polishing a modified buffered chemical polishing (BCP) at the vendor site was applied. As the frequency of cavities is highly sensitive to the amount of the removed material (about 10 kHz per 1 μm removed) we aimed to etch away as little material as reasonably possible. To reduce the etching rate for better control of the process the BCP solution of 1:1:4 was used [8]: 1 volume of 48% HF, 1 volume of 65% HNO_3 and 4 volumes of 85% H_3PO_4 as a buffer solution. Varying the level of H_3PO_4 thus affects the etching rate the mixture was cooled before and during the etching process by an ice-cooled water bath. Temperature sensor installed on the outer surface cavity beam tube showed temperature in the range of 10 °C–12 °C during the etching process.

The average amount of material removed was deduced by weighing the dry cavity before and after the treatment. In addition, the material removal rate by the acid was checked twice, before and during the cavity treatment, by means of a sample. To calculate the removal rate, a flat rectangular niobium sample with a known surface area was etched in the BCP solution for two minutes. Weighing the sample before and after the etching allowed the determination of the etching speed.

Gun 1.0 was used as a test piece and etched with BCP twice. After the first removal of about 0.9 μm (on average) a matte area around the cathode opening was observed. The cavity received a further etch, with about 5.7 μm removed.

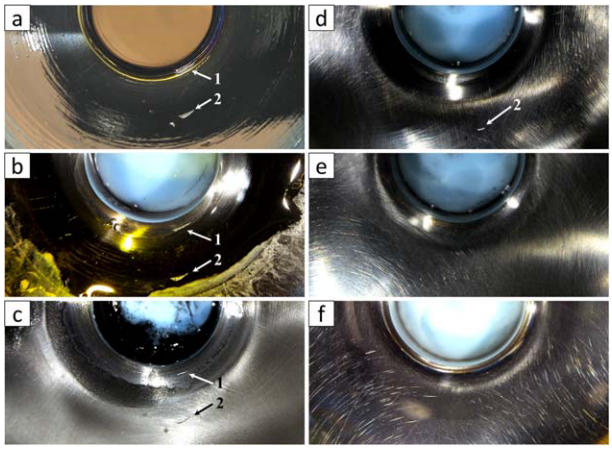

Figure 15. Optical images of the back plane surface of Gun 1.0 after different polishing steps. Defects #1 and #2 are indicated with arrows. Figure (a) shows the original surface with the defects marked by #1 and #2. Figures (b), (c), (d) and (e) show the surface at different stages of rough polishing. Figure (f) shows the final surface after the full polishing process. In figure (b) some slurry from the polishing is still visible.

Gun 1.1 received a single BCP etch, with 4.5 μm niobium removed. However due to a mistake during acid preparation, a 1:1:8 mixture was used, resulting in longer etching times.

After BCP each cavity received an HPR as employed for European XFEL cavities was then transported to HZB for the cold test.

8. High pressure rinsing

The first cold test of Gun 1.0 after the polishing showed improved quality factor but suffered from a low field-emission onset field at about 7 MV/m (see top plot in figure 16).

The onset field of the field emission was increasing during the test (all three curves 'After Polishing' are acquired during one cold test) in comparison to the field emission we saw before polishing. That was by a hard, material damage caused defect, which means it cannot be processed by RF field, such that it will physically remain in its geometrical emission location. The field emitter is mainly caused by a local deformation of the surface leading to an intensified local electric field allowing the lower field emission onset compared to a flat surface. But field emission after the polishing and etching was not stable and changed with RF processing, as indicated by the shifting Q_0 curves. It became evident that its source was not a hard defect. This was verified by improving the field-emission onset after an additional in-house HPR at HZB. We assumed that it may have been remnants of the polishing process on the back-wall and in the cathode channel which were not cleaned or removed properly by existing HPR nozzle arrangement.

Based on the performance data it was concluded that a new HPR nozzle is required: a standard HPR nozzle used for TESLA-type cavities doesn't clean the back plate of the gun cavity. For that reason, we developed the so-called 'Gun nozzle', as shown in figure 17: the stainless-steel body holds 10 screw-in nozzles (produced by Spraying Systems Co., not shown in the picture). As compared to the standard nozzle head it has additional water jets towards the back plate of the gun cavity. Using such a nozzle head yielded a significant improvement in the FE onset field (see bottom plot in figure 16). For Gun 1.1 it shifted the onset field from about 10 MV m^{-1} after standard HPR to about 16 MV m^{-1}.

The Gun nozzle was also used for rinsing of the choke side of the cavity as it was feared, the particulates can migrate from the reasonably 'dirty' choke cell into the main cavity. However, the choke cell can be rinsed only through a small gap close to the cathode opening. For this reason, we also developed a so-called 'choke-cell nozzle' shown in figure 18. It is small enough to pass through the cathode opening and has ten jets with different angles. Moving through the opening it sprays the choke cell with different jets cleaning the whole surface.

However the use of the choke-cell nozzle caused an intensive colorization of the cathode opening and the back plate close to the cathode (see figure 19). This intense colour is known to be caused by the light interference in thick niobium oxide [19, 20]. In figure 19(b) one still sees the ring from the damage. This is no longer a scratch but change in reflection after chemical treatment. Although cavities showed good performance in cold tests, we decided to remove the excessive oxide layer which might lead to unpredictable effects (in particular multipacting) during photoinjector operation when the cathode is inserted. For this purpose we performed an

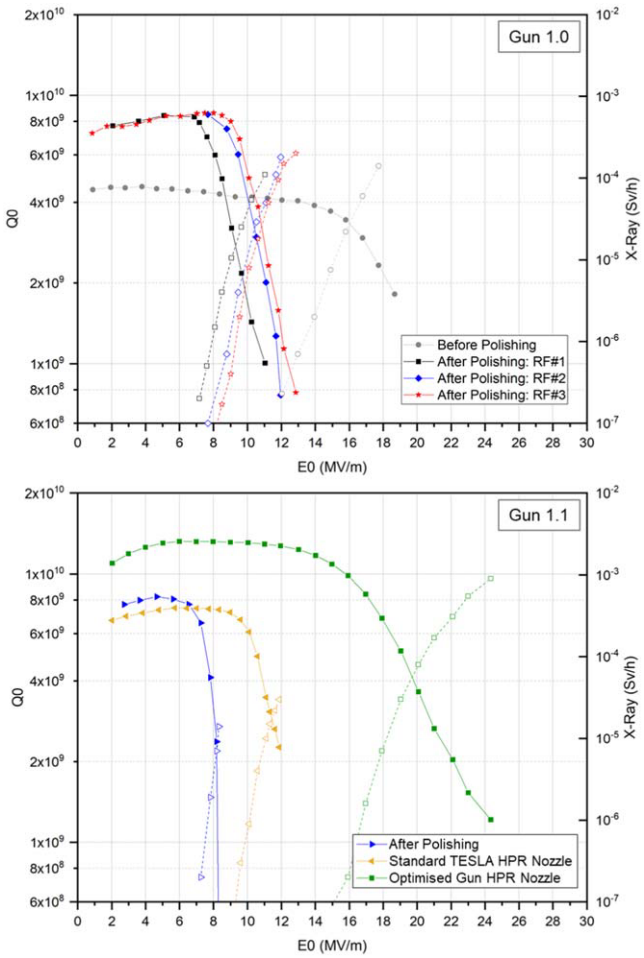

Figure 16. Top: Gun1.0 performance before and after the polishing (with BCP and standard HPR). Bottom: Gun 1.1 performance after the polishing (with BCP and standard HPR), after additional standard HPR and after HPR with the Gun nozzle. Dashed lines represent field emission.

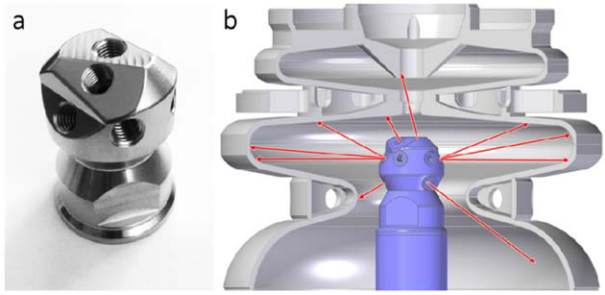

Figure 17. The Gun nozzle designed to rinse the photoinjector cavities (a) and its water-jet pattern (b).

additional study of the material in colorized regions (see section 9) and developed a retreatment procedure (see section 10).

After removal of the oxide layer by rinsing with hydrofluoric acid, only the gun-nozzle was used to clean both sides (main-cell side and choke-cell side) of the cavity. So far, the choke-cell nozzle has not been used again for these cavities, but it is planned to further optimize the HPR parameters in the future to avoid the discoloration with this system for maximum cavity performance.

The following parameters were used for all HPR runs. The water pressure was 100 bar, the cavity made two turns per minute and vertical translation of the cavity was 10 mm per minute. In addition, filtered nitrogen gas (filter's particle removal rating $\geqslant 3$ nm) was supplied through the lance. As it will be shown in the following section, a reliable electrical grounding of the cavity is critical.

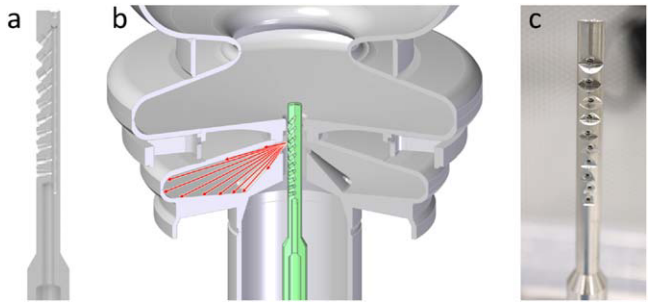

Figure 18. Choke-cell nozzle design (a), its water-jet pattern inside the choke-cell (b) and photo image of the nozzle (c).

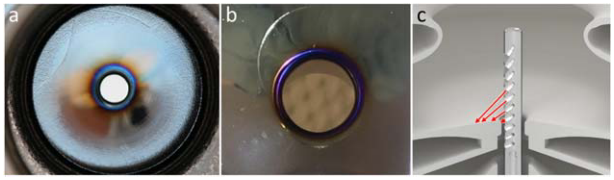

Figure 19. Colorization of the Nb surface around the cathode opening in Gun1.0 (a) and Gun1.1 (b) and a schematic image of the water jets that presumably were the cause of the discoloration (c).

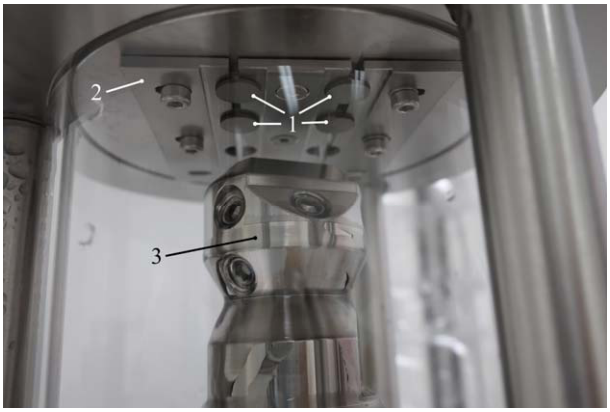

Figure 20. Nb coupons (1) in a holder (2) above the Gun nozzle (3).

As the main-cell side is the most critical part of the cavity it must be cleaned more thoroughly. We cleaned the main cell side first, then the choke-cell side (after flipping the cavity) and the main cell side again. The capacity of our ultrapure water (UPW) storage system was not enough to complete this sequence in one run. After several experiments we established the following procedure. The cavity gets one or two cleaning cycles on the main cell side and right after that, one or two cycles on the choke-cell side. Then the cavity stays overnight, until the UPW system is refilled and the next day it gets six cycles on the choke cell side and the final six cycles on the main cell side. Thus the main cell is rinsed the last.

9. Study of the impact of HPR on niobium

To find the proper HPR parameters and especially a safe nozzle-to-surface distance, additional studies with Nb samples ('coupons') were performed. Several small (about 8 mm in diameter) coupons made of fine-grain Nb sheets were placed in a holder to represent a back wall of the gun (see figure 20). During the coupon tests it was also discovered that the cavity holder in our HPR system was not reliably grounded: whenever the ground connection was lost during the operation, strong oxidation of the coupons occurred.

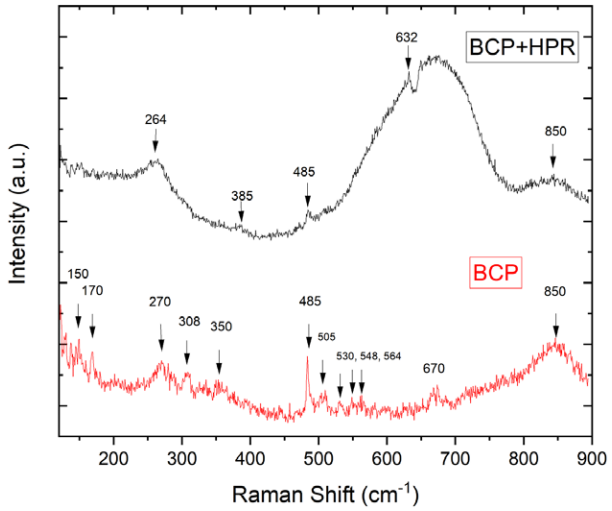

Figure 21. The Raman Spectra ($\lambda = 532$ nm) of niobium after BCP (bottom line) and after BCP followed by HPR (top line).

The coupons received an HPR with the same settings as the cavities that oxidized to identify a proper surface treatment procedure.

9.1. Material analysis of coupons

The x-ray photoelectron spectroscopy (XPS) of niobium coupons was performed at the dipole beamline RGBL, BESSY II synchrotron-radiation facility (HZB, Berlin) at photon-beam energies of 450–1000 eV and normal-emission geometry at a 55° angle between the incident beam and the analyzer aperture. The binding-energy (BE) scale of the spectra was calibrated using the Au $4f_{7/2}$ core-level peak located at 84.0 eV measured with a metal foil. The spectra processing was performed using the CasaXPS software package using the fitting model described in [21].

The samples were additionally characterized by SEM, XRD (Bruker D8 Advance, Cu K-α), and Raman spectroscopy (MonoVista SP-2500i, 532 nm DPSS-laser, 5 mW). In order to choose the method of removing the defective structure created by HPR, it is necessary to determine the chemical state of the created film. Since Raman frequencies strongly depend on the niobium oxide structures, this technique has been employed to investigate the colored film observed on niobium coupons as well as the gun cavity after the HPR.

9.1.1. Raman spectroscopy

In figure 21 the Raman spectra of niobium surface after the standard BCP as well as the one subjected to HPR are presented for comparison. The former spectrum contains the Raman bands at 150, 170, 270, 308, 350, 485, 530, 548, 564, 670, and 850 cm^{-1}, that were reported for Nb-O modes of vibration in the slightly distorted [NbO_6] octahedra as well as among the octahedra in various polymorphs of Nb_2O_5 [22–24].

The spectrum collected from the niobium coupon subjected to HPR in the area where the blue colour was the most intense, reveals the Raman bands at 264, 385, 485, 632, 670 and 850 cm^{-1}. The bands at stretching frequencies 264, 485, 850 cm^{-1} were observed in Nb_2O_5 [22, 23] while at 632 cm^{-1} was reported for both Nb_2O_5 [22] and NbO_2 [25]. One should note that in [25] the XPS spectra revealed the presence of Nb^{+5} oxidation state in the NbO_2 (Nb^{+4}) material. A broad and strong Raman band at ~650 eV is a typical feature of amorphous niobium oxide Nb_2O_5 or/and its hydrated form $Nb_2O_5{\cdot}n(H_2O)$ that possesses distorted [NbO_6] octahedra, [NbO_7] pentahedra and [NbO_8] hexahedra as structural units [24, 26, 27].

9.1.2. X-ray photoelectron spectroscopy

To further characterize the aforementioned oxide films an XPS study has been performed. The wide-range survey XPS spectra of the BCP-ed and HPR-ed niobium surface were represented by the core-level transitions specific to niobium, oxygen and carbon. For the both samples, C 1*s* core-level (~285 eV) was represented by carbonaceous adsorbate commonly found at the surfaces of solids after exposure to air (not shown).

The Nb 3*d* and O 1*s* core-level regions of the niobium coupons processed with HPR and following an HF-rinsing are presented in figures 22(a), (b) and figures 22(c), (d), respectively. O 1*s* was fitted with three contributions: 530.6, 531.5 and 532.7 eV associated with O^{-2}-ions in niobium oxides, low-coordination-number O^{-1}-ions that are compensating for some deficiencies in the oxide subsurface [28], and weakly adsorbed species such as aliphatic C–O–C, etc [29], correspondingly.

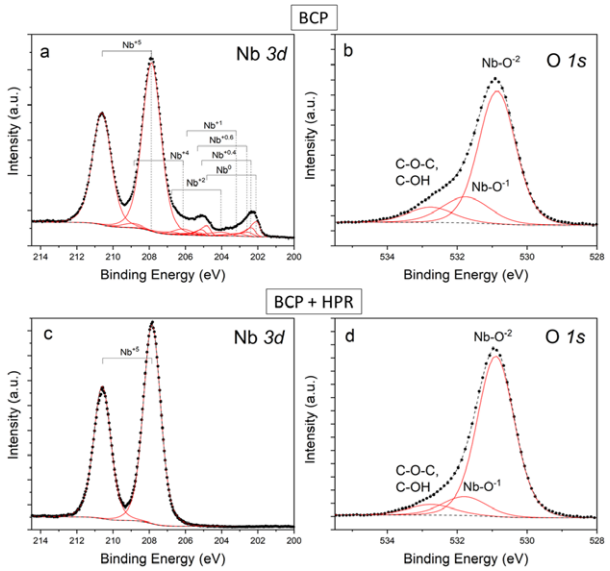

Figure 22. High-resolution energy dispersion curves of Nb3*d* and O1*s* regions of the BCP-ed (a), (b) and HPR-ed (c), (d) niobium surface, respectively, collected at $h\nu = 1000$ eV.

The Nb 3*d* and O 1*s* core-levels (figures 22(a), (b) collected from the BCP-ed niobium underscores the predominant Nb^{5+}-oxidation state with the Nb $3d_{5/2}$-binding energy at 207.85 eV and the small contributions from the lower niobium valences in the oxide film, evidently, located at the border with the metallic niobium, Nb^0 (Nb $3d_{5/2}$ at 202.05 eV). For the blue niobium area after the HPR, only the doublet of Nb^{5+} state was pronounced with the same binding energy of Nb $3d_{5/2}$ as for the BCP-ed niobium (figures 22(c), (d). Thus, the presence of Nb^{+4} corresponding to NbO_2 is ruled out. The FWHMs of the Nb 3*d* doublets corresponding to Nb^{+5} was slightly broader for the BCP-ed niobium surface (1.24 eV) as compared to the blue area obtained by HPR (1.15 eV). It is probably related to the Nb_2O_5-thickness difference of the two samples, and the tension that occurs at the border with metallic niobium which is disturbed in the case of BCP. The calculated 90%-information depth (the depth normal to the surface from which 90% of the detected signal originates [30]) for our experimental condition is 4.64 nm ($h\nu = 1000$ eV).

X-ray diffraction measurements both in Bragg–Brentano geometry and at small angles of incidence of primary beam revealed no reflexes except niobium, which proves the amorphous structure of the film. Thus, from the presented data analysis we conclude that the blue-coloured film observed at the niobium surface after HPR represents the amorphous Nb_2O_5. It is known that Nb_2O_5 can be etched away with the diluted water solution of HF acid [31].

10. Hydrofluoric acid rinsing

To understand the reason for a strong oxidation and to find a suitable treatment for cavities the same Nb coupons were used to reproduce the defect. In the left part of figure 23(a) coupon with strong oxidation caused by HPR is shown. In the right one can see the same coupon after treatment by 5% hydrofluoric acid for 10 min.

After coupon studies, a hydrofluoric acid rinsing (HF rinsing) procedure was applied to remove the oxide from the cavity surface. A simple setup shown in figure 24 was developed to perform chemical treatment of the cavities. It consists of a membrane pump, valves, hoses, cavity flanges and 10 litre acid canister. All components are made of polytetrafluoroethylene (PTFE) or polypropylene (PP). Viton (FKM) gaskets are used to seal cavity flanges. A pressurized air driven pump allows filling and draining the cavity as well as acid circulation during treatment.

A water solution of hydrofluoric acid (5% by volume) was used. This mixture reacts only with niobium pentoxide. As the total amount of niobium oxide is negligible compared to the mixture volume there is no detectable heating of the mixture or the cavity. As a result, an additional heat exchanger is not required and the acid was at room temperature during the treatment (from 19 °C to 21 °C).

The setup was placed in a standard chemical fume cabinet. It was not necessary to keep the acid circulation as no gas evolves during the treatment. The pump was running for two minutes every five minutes of treatment. After treatment was completed, the acid was pumped out of the cavity to the acid canister and ultrapure water rinsing began. UPW was supplied with the flow of about 5 l min^{-1}. The resistivity of drain water was

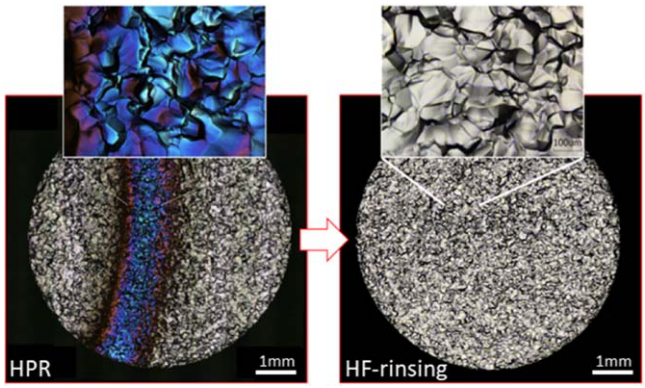

Figure 23. Optical image of Nb coupon after HPR with too short distance between nozzle and sample (left) and the same coupon after HF rinsing (right).

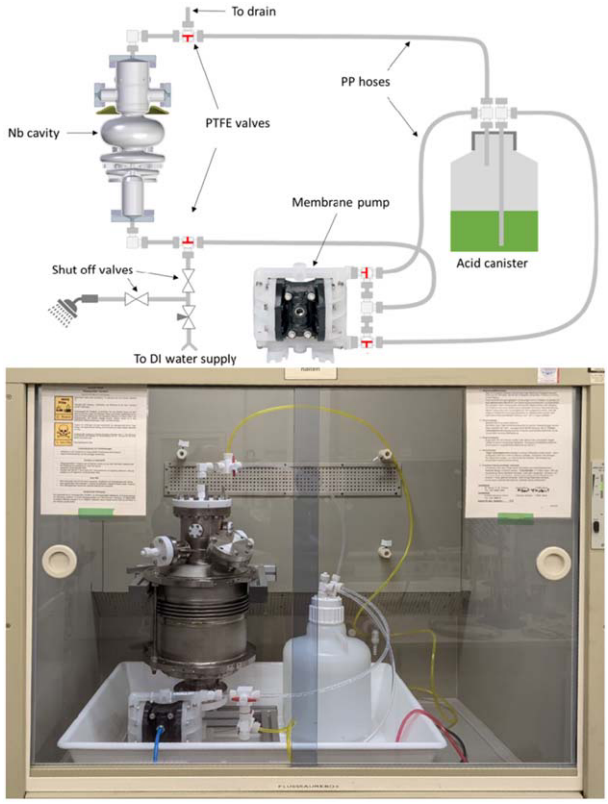

Figure 24. Diagram (top) and image (bottom) of a setup used for HF rinsing.

continuously measured and rinsing was stopped when it reached 100 kΩ cm. Afterwards the water was drained and the cavity was transported in to the clean room for ultrasound cleaning and HPR.

In Gun 1.0 the colour layer was completely removed after 30 min of HF rinsing,while for Gun 1.1 it took 150 min in 3 steps: 30 min, 60 min and 60 min. This suggests that the oxide layer in Gun 1.1 was much thicker. After each step the cavity was rinsed with ultra-pure water and checked in the clean-room. Typical images of the surface before and after HF rinsing are shown in figure 25.

11. Final cavity performance and summary

Figure 26 shows the cavities' performance after each treatment step. All tests shown were performed without 120 °C baking of the cavity, as it was not critical for intermediate steps.

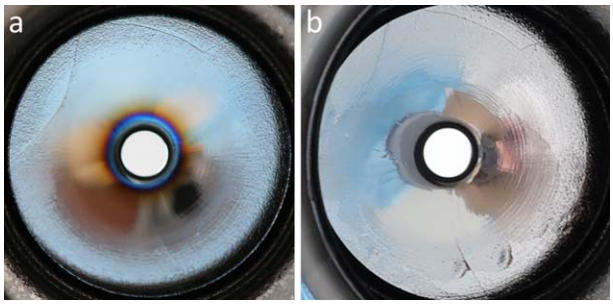

Figure 25. Optical image of the back plate of Gun1.0 after HPR with a choke-cell nozzle (a) and after subsequent HF rinsing.

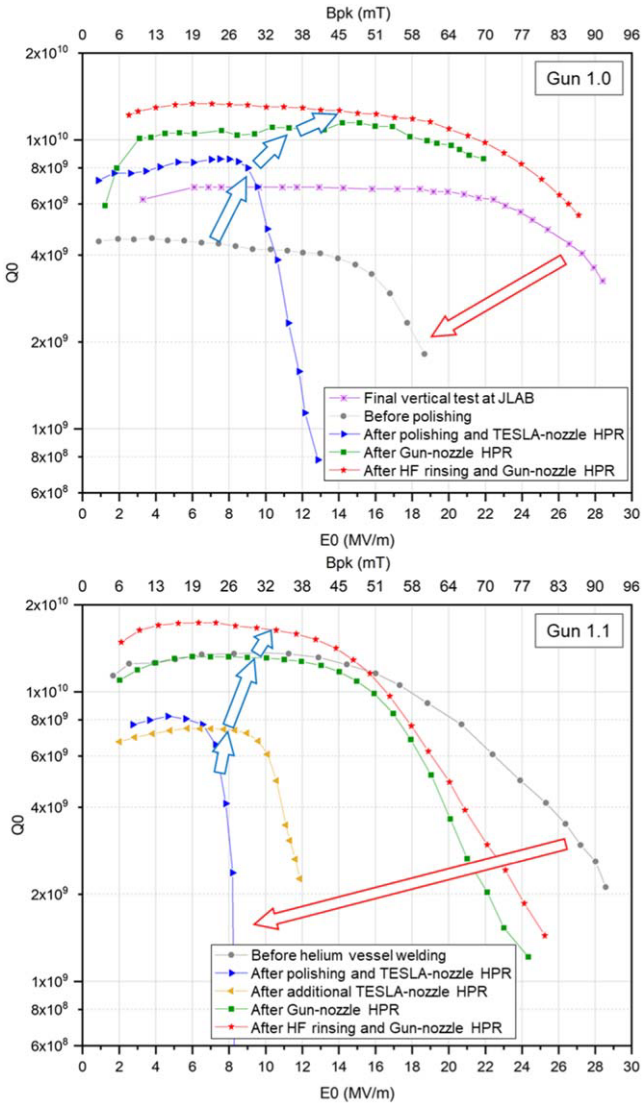

Figure 26. Evolution of Gun 1.0 (top) and Gun 1.1 (bottom) performance.

As one can see, performance of Gun 1.0 is significantly improved compared to initial performance: Q_0 is twice higher and no field emission up to maximum field. In case of Gun 1.1 the low field Q_0 slightly increased, but high-filed Q_0 is lower, but no field emission observed. It should be noted that the baseline test for Gun 1.1 was performed after 120 °C treatment while it was omitted in the final test. Also this cavity received only 650 °C annealing during production, so it is possible that the amount of hydrogen in niobium after the full treatment increased and reached the level, when Q-disease is pronounced. It is planned to apply 800 °C annealing followed by light BCP to this cavity during injector module refurbishing.

As a result we demonstrated the first time a full recovery of a damaged SRF photoinjector cavities, which were not able to be operated because of a huge defects in the high electric field cathode area, and could bring them back to original level. It took two years as a series of tools needed to be adapted for the specific cavity shape or completely developed. Because we only have two photoinjector cavities and the goal was to recover both, we had to carefully design and test each treatment step and evaluate its effect on cavity perfomance before we could implement such a treatment.

Acknowledgments

We acknowledge Andrew Burrill and Axel Matheisen for fruitfull discussions. Axel Hellwig, Karsten Janke, Stefan Rotterdam and Svenja Heling are particularly acknowledged for the operation of cryogenics. We express special thanks to Anna Makarova and Dmitry Smirnov for their help in making measurements on RGBL beamline at BESSY II.

Data availability statement

All data that support the findings of this study are included within the article (and any supplementary files).

ORCID iDs

Yegor Tamashevich https://orcid.org/0000-0003-0608-6485
Alena Prudnikava https://orcid.org/0000-0003-0647-2546

References

[1] Neumann A *et al* 2016 Final acceptance test of the srf photo-injector cold string for the berlinpro energy recovery linac *In 28th Int. Linear Accelerator Conf.(LINAC'16), East Lansing, Michigan, USA*
[2] Neumann A, Anders W, Kamps T and Jülich E Z F 2012 *Photoinjector SRF Cavity Development for BERLinPro* (LINAC12)
[3] Conway Z A and Liepe M U 2009 Fast piezoelectric actuator control of microphonics in the CW Cornell ERL injector cryomodule *Particle Accelerator Conference PAC 2009 (Vancouver, BC, Canada)* 918–920
[4] Kugeler O, Neumann A, Anders W and Knobloch J 2010 Adapting TESLA technology for future cw light sources using HoBiCaT *Rev. Sci. Instrum.* **81** 074701-1–074701-9
[5] Neumann A, Anders W, Burrill A, Frahm A, Kamps T and Jülich E Z F 2013 SRF Photoinjector Cavity for bERLin-Pro *International Particle Accelerator Conference IPAC 2013 (Shanghai, China)* 285
[6] Arnold A *et al* 2007 Development of a superconducting radio frequency photoelectron injector *Nucl. Instrum. Methods Phys. Res., Sect. A* **577** 440–54
[7] Neumann A *et al* 2018 The bERLinPro SRF photoinjector system-from first RF commissioning to first beam *In 9th Int. Particle Accelerator Conf.(IPAC'18), Vancouver, Canada*
[8] Padamsee H, Knobloch J and Hays T 1998 *RF Superconductivity for Sccelerators* (Wiley)
[9] Neumann A 2023 Experimental and simulated dark current and beam loss studies for a SRF photo-injector of an ERL injector *(THPL044) In 14th Int. Particle Accelerator Conf.(IPAC'23) Venice, Italy*
[10] Schmeißer M A, Mistry S, Kirschner H, Schubert S, Jankowiak A, Kamps T and Kühn J 2018 Towards the operation of Cs-K-Sb photocathodes in superconducting rf photoinjectors *Phys. Rev. Accel. Beams* **21** 113401
[11] Kneisel P, Lewis B and Turlington L 1993 Experience with high pressure ultrapure water rinsing of niobium cavities *Proc. of The Sixth Workshop on RF Superconductivity* (CEBAF) 628–36
[12] Kneisel P and Lewis B 1996 Advanced surface cleaning methods-three years of experience with high pressure ultrapure water rinsing of superconducting cavities *Part. Accel.* **53** 97–121
[13] Ge M, Wu G, Burk D, Ozelis J, Harms E, Sergatskov D, Hicks D and Cooley L D 2010 Routine characterization of 3D profiles of SRF cavity defects using replica techniques *Supercond. Sci. Technol.* **24** 035002
[14] Xu C, Reece C and Kelley M 2013 Characterization of Nb SRF cavity materials by white light interferometry and replica techniques *Appl. Surf. Sci.* **274** 15–21
[15] Navitski A, Elsen E, Foster B, Laasch R, Reschke D, Schaffran J, Singer W, Singer X and Tamashevich Y 2013 R&D on cavity treatments at DESY towards the ILC performance goal *In Proc. SRF* 2013
[16] Matheisen A, Horst B, Steinhau-Kühl N, Krupka N, Schilling P and Saegebarth S 2015 Experience on retreatment of EUXFEL series cavities at DESY *In Proc. International Conference on RF Superconductivity SRF2015* 296
[17] Monaco L, Michelato P, Pagani C, Navitski A, Schaffran J, Singer W, Prudnikava A and Tamashevich Y 2015 Study of the evolution of artificial defects on the surface of niobium during electrochemical and chemical polishing *In Proc. SRF* 2015
[18] Bjerregaard L, Geels K, Ottesen B and Ruckert M 2000 *Struers Metalog Guide* (Struers A/S)
[19] Knobloch J and Freyman R 1998 *Effect of high-pressure rinsing on niobium. SRF Note,* 980223–01 (https://classe.cornell.edu/public/SRF/1998/SRF980223-01/SRF980223-01.pdf)
[20] Sertore D, Fusetti M, Michelato P, Pagani C and Pierini P 2006 High pressure rinsing water jet characterization *Proc. EPAC06, INFN Milano-LASA, Segrate (MI), Italy*
[21] Prudnikava A, Tamashevich Y, Babenkov S, Makarova A, Smirnov D, Aristov V, Molodtsova O, Kugeler O, Viefhaus J and Foster B 2022 Systematic study of niobium thermal treatments for superconducting radio frequency cavities employing x-ray photoelectron spectroscopy *Supercond. Sci. Technol.* **35** 065019

[22] Huang B X, Wang K, Church J S and Li Y S 1999 Characterization of oxides on niobium by raman and infrared spectroscopy *Electrochim. Acta* **44** 2571–7
[23] McConnell A A, Aderson J S and Rao C N R 1976 Raman spectra of niobium oxides *Spectrochimica Acta Part A: Molecular Spectroscopy* **32** 1067–76
[24] Hardcastle F D and Wachs I E 1991 Determination of niobium-oxygen bond distances and bond orders by Raman spectroscopy *Solid State Ionics* **45** 201–13
[25] Wang Y, Comes R B, Kittiwatanakul S, Wolf S A and Lu J 2015 Epitaxial niobium dioxide thin films by reactive-biased target ion beam deposition *Journal of Vacuum Science & Technology A* **33** 021516-1–021516-5
[26] Jehng J M and Wachs I E 1991 Structural chemistry and raman spectra of niobium oxides *Chem. Mater.* **3** 100–7
[27] Graça M P F, Saraiva M, Freire F N A, Valente M A and Costa L C 2015 Electrical analysis of niobium oxide thin films *Thin Solid Films* **585** 95–9
[28] Dupin J C, Gonbeau D, Vinatier P and Levasseur A 2000 Systematic XPS studies of metal oxides, hydroxides and peroxides *Phys. Chem. Chem. Phys.* **2** 1319–24
[29] Beamson G and Briggs D J M P 1992 High resolution monochromated x-ray photoelectron spectroscopy of organic polymers: a comparison between solid state data for organic polymers and gas phase data for small molecules *Mol. Phys.* **76** 919–36
[30] Powell C J and Jablonski A 2010 Progress in quantitative surface analysis by x-ray photoelectron spectroscopy: Current status and perspectives *J. Electron. Spectrosc. Relat. Phenom.* **178** 331–46
[31] Lidin R A, Molochko V A and Andreeva L L 2007 *Reactions of Inorganic Substances* (Drofa)